

Large Chinese land carbon sink estimated from atmospheric carbon dioxide data

<https://doi.org/10.1038/s41586-020-2849-9>

Received: 2 March 2018

Accepted: 26 August 2020

Published online: 28 October 2020

 Check for updates

Jing Wang^{1,2,3,4}, Liang Feng^{3,4}, Paul I. Palmer^{3,4}, Yi Liu^{1,2}, Shuangxi Fang^{5,6}, Hartmut Bösch⁷, Christopher W. O'Dell⁸, Xiaoping Tang⁹, Dongxu Yang^{1,2}, Lixin Liu⁶ & ChaoZong Xia⁹

Limiting the rise in global mean temperatures relies on reducing carbon dioxide (CO₂) emissions and on the removal of CO₂ by land carbon sinks. China is currently the single largest emitter of CO₂, responsible for approximately 27 per cent (2.67 petagrams of carbon per year) of global fossil fuel emissions in 2017¹. Understanding of Chinese land biosphere fluxes has been hampered by sparse data coverage^{2–4}, which has resulted in a wide range of a posteriori estimates of flux. Here we present recently available data on the atmospheric mole fraction of CO₂, measured from six sites across China during 2009 to 2016. Using these data, we estimate a mean Chinese land biosphere sink of -1.11 ± 0.38 petagrams of carbon per year during 2010 to 2016, equivalent to about 45 per cent of our estimate of annual Chinese anthropogenic emissions over that period. Our estimate reflects a previously underestimated land carbon sink over southwest China (Yunnan, Guizhou and Guangxi provinces) throughout the year, and over northeast China (especially Heilongjiang and Jilin provinces) during summer months. These provinces have established a pattern of rapid afforestation of progressively larger regions^{5,6}, with provincial forest areas increasing by between 0.04 million and 0.44 million hectares per year over the past 10 to 15 years. These large-scale changes reflect the expansion of fast-growing plantation forests that contribute to timber exports and the domestic production of paper⁷. Space-borne observations of vegetation greenness show a large increase with time over this study period, supporting the timing and increase in the land carbon sink over these afforestation regions.

The global mass and growth of atmospheric CO₂ can be determined by surface-based measurements (www.esrl.noaa.gov/gmd/ccgg/trends/). The largest anthropogenic emissions of CO₂ include fossil fuel combustion, cement production and human-driven changes to land use¹. Reconciliation of bottom-up emission estimates of these anthropogenic processes, accounting for widely assumed uncertainties, with atmospheric CO₂ measurements reveals a surprisingly invariant airborne fraction of $44 \pm 14\%$ ⁸. The remainder is absorbed by the ocean and land biosphere⁹. Sparse measurements of partial pressure of CO₂ in the surface ocean, p_{CO_2} , taking advantage of large-scale spatial–temporal correlations, allow estimation of ocean CO₂ fluxes¹⁰, although regional campaigns highlight large flux variations in successive years¹¹. The residual of these mass balance terms yields the magnitude of the land biosphere carbon balance⁹. Current understanding of the land biosphere, encapsulated in numerical models, requires additional uptake to be reconciled with the data-driven residual term, even accounting for uncertainties¹. Therein lies the crux of the challenge faced by the science and policy communities: effective mitigation of fossil fuel CO₂ emissions within a large-scale, dynamic natural carbon cycle that we do not quantitatively understand.

China overtook the United States in 2006 as the single largest emitter of CO₂, mainly due to the fossil fuel combustion and cement production

sectors¹². These emission estimates have large uncertainties¹³ that translate into larger uncertainties for residual terrestrial biosphere flux estimates^{2,3} (see Methods). Sparse in situ observations over China result in a large model spread of a posteriori terrestrial fluxes estimates^{2,3,14}, with values highly sensitive to available data⁴.

Constraints on CO₂ flux estimates

In this study, we use newly available in situ CO₂ mole fraction data (collectively describing weekly flask and hourly continuous measurements) over China (see Methods section ‘Data’ and Supplementary Information; Extended Data Fig. 1) from 2009 to 2016 to show how these data can revise the provincial and national carbon balance of China. We corroborate our unexpected a posteriori flux estimates through independent satellite remote-sensing measurements of vegetation greenness, soil water availability, a posteriori fluxes inferred from satellite column observations of CO₂, and consecutive Chinese forest censuses.

We use several sources of data to investigate the Chinese carbon balance (see Methods and Supplementary Information): in situ measurements of CO₂ mole fraction, satellite column observations of CO₂, leaf area index (LAI), normalized difference and enhanced vegetation

¹Institute of Atmospheric Physics, Chinese Academy of Sciences, Beijing, China. ²University of Chinese Academy of Sciences, Beijing, China. ³National Centre for Earth Observation, University of Edinburgh, Edinburgh, UK. ⁴School of GeoSciences, University of Edinburgh, Edinburgh, UK. ⁵College of Environment, Zhejiang University of Technology, Hangzhou, China. ⁶Meteorological Observation Centre, China Meteorological Administration, Beijing, China. ⁷National Centre for Earth Observation, University of Leicester, Leicester, UK. ⁸Colorado State University, Fort Collins, CO, USA. ⁹Academy of Forest Inventory and Planning, State Forestry Administration, Beijing, China. ¹⁰e-mail: paul.palmer@ed.ac.uk; liuyi@mail.iap.ac.cn; fangsx@cma.gov.cn

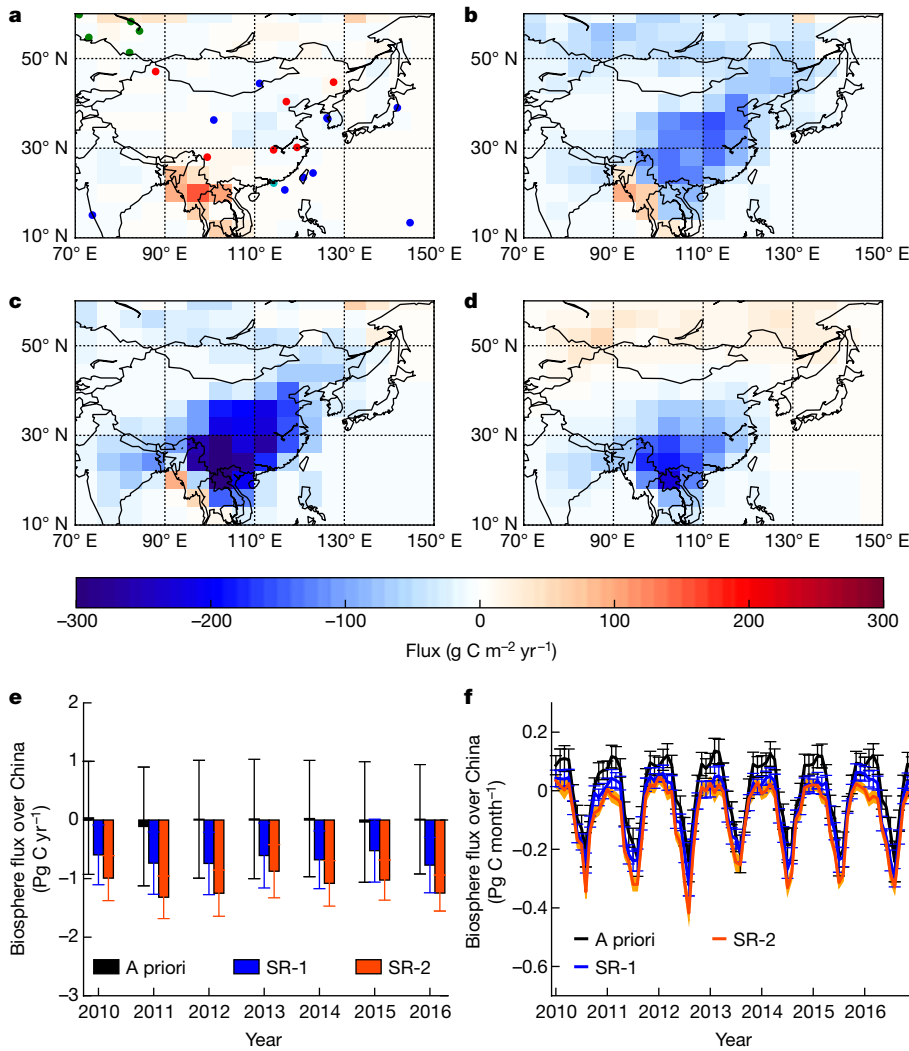


Fig. 1 | Chinese terrestrial biosphere CO₂ fluxes. **a–c**, Annual mean spatial distributions of CO₂ fluxes (g C m⁻² yr⁻¹) for 2010–2016 (inclusive) corresponding to the a priori inventory (**a**) and to a posteriori CO₂ fluxes corresponding to SR-1 (**b**) and SR-2 (**c**). **d**, Difference between SR-2 and SR-1 (g C m⁻² yr⁻¹). In **a**, the blue, cyan, green and red dots denote NOAA ObsPack stations, the Hok Tsui (HKG) station from World Data Centre for Greenhouse Gases (WDCGG), Japan–Russia Siberia Tall Tower Inland Observation Network and the China Meteorological Administration (CMA) regional background stations, respectively. **e**, Annual CO₂ fluxes from the a priori inventory, and a posteriori fluxes inferred from (SR-1) NOAA ObsPack CO₂ mole fraction measurements, and (SR-2) NOAA + Siberian + CMA + HKG CO₂ mole fraction measurements from 2010 to 2016, inclusive. **f**, Corresponding monthly fluxes. In **e** and **f**, vertical bars and the orange envelope denote a priori and a posteriori uncertainties.

indices (NDVI and EVI, respectively), liquid water equivalent thickness derived from gravity anomalies, and above-ground biomass inferred from microwave measurements. The atmospheric data are interpreted using the GEOS-Chem atmospheric transport model coupled with a Bayesian inversion tool to infer CO₂ fluxes from the atmospheric data (see Methods).

CO₂ fluxes inferred from atmospheric data

First, we use an atmospheric inversion to estimate the magnitude and distribution of land biosphere CO₂ fluxes over China (see Methods). Inversion SR-1, which uses only the ObsPack GLOBALVIEWplus data (Fig. 1a) provided by the Earth System Research Laboratory (ESRL) of the National Oceanic and Atmospheric Administration (NOAA), shows a CO₂ sink over most of China (Fig. 1b), mainly focused over central, northeast and southern China. These data are consistent with a mean annual net uptake estimate for the terrestrial biosphere of -0.66 ± 0.52 petagrams of carbon per year (Pg C yr⁻¹; 2010–2016), varying from -0.52 ± 0.54 Pg C yr⁻¹ in 2015 to -0.77 ± 0.47 Pg C yr⁻¹ in 2016 (Fig. 1e, Table 1). We find that the annual Chinese carbon sink is mostly due to uptake during the growing season, particularly during June to August (Fig. 1f).

Including the Siberian tower data (see Data and Supplementary Table 1) broadly increases CO₂ uptake over China and India. The additional Chinese mainland sites (Extended Data Fig. 1), together with the Siberian and Hong Kong data, in inversion SR-2 (Fig. 1c) have two major impacts on our understanding of the Chinese carbon budget. First, these data bring into sharper focus the distribution of Chinese CO₂

fluxes (Fig. 1c), increasing the net uptake over the southwest (mainly Yunnan, Guizhou and Guangxi provinces), and increasing net emissions over the northeast (mainly Heilongjiang, Jilin and Liaoning provinces) relative to SR-1 (Fig. 1d). Second, the resulting uncertainties of the Chinese CO₂ budget are also much smaller than when using only the NOAA ObsPack data (Fig. 1f, Supplementary Fig. 6).

Table 1 reports annual CO₂ fluxes for China. Using inversion SR-2, we find that the mean annual Chinese land biosphere sink is -1.11 ± 0.38 Pg C yr⁻¹ over 2010–2016. The magnitude of this sink term is 68% larger than the a posteriori values inferred from SR-1 for the same period (-0.66 ± 0.52 Pg C yr⁻¹), with uncertainties reduced by about 27% (Fig. 1f, Table 1; Supplementary Fig. 6). This revised sink term is substantially larger (that is, more uptake) than many recent estimates^{3,4,14–18} that cover various periods between 1980 and 2013 and inferred using different methods and data, including the inversion of atmospheric data (Table 1).

Our a posteriori estimate of CO₂ uptake over southwest China (18–30° N, 95–110° E) accounts for about 32% of the uptake over the Chinese mainland. We also find evidence of substantial year-to-year variability of carbon uptake across southwest China (Fig. 2a, b), with the largest values during boreal summer months. As we discuss below, this variation is at least partly due to the young age structure of this forest ecosystem^{5,19,20} and variations in meteorology (Supplementary Fig. 13). The relatively smaller uptake over northeast China (compared with SR-1) is due to the elevated sink during the growing season (Fig. 2c, d, Extended Data Fig. 2) that is compensated by emissions during the rest of the year.

Table 1 | Carbon dioxide fluxes over China and East Asia

This study (Pg C yr ⁻¹)			Previous studies (Pg C yr ⁻¹)			
Year	SR-1	SR-2	Method	Period	Carbon balance	Reference
2010	-0.60 ± 0.51	-0.99 ± 0.38	Inventory-satellite-based or process-based model estimation	1961–2005	-0.179 ^a	16
2011	-0.74 ± 0.53	-1.32 ± 0.36		1980–1999	-0.177 ± 0.073 ^b	15
2012	-0.74 ± 0.53	-1.25 ± 0.39		1990–2009	-0.224 ± 0.141 ^{b,c}	14
2013	-0.61 ± 0.55	-0.87 ± 0.45		2001–2010	-0.966 ^b	18
2014	-0.68 ± 0.49	-1.08 ± 0.39		2006–2009	-0.33 ^b	4
2015	-0.52 ± 0.54	-1.03 ± 0.34	Atmospheric inversion	1996–2005	-0.35 ± 0.33 ^a	15
2016	-0.77 ± 0.47	-1.25 ± 0.31		1990–2009	-0.270 ± 0.507 ^{b,c}	14
				2001–2010	-0.33 ^a	17
				2008–2012	-0.46 (-1.18 to -0.01) ^{a,c,d}	3
				2006–2009	-0.45 ^a	4
2010–2016 mean	-0.66 ± 0.52	-1.11 ± 0.38				

In this study, inversion SR-1 denotes NOAA ObsPack in situ data (including one site over China); inversion SR-2 denotes in situ data from NOAA ObsPack, Siberia, Hong Kong and from the Chinese mainland. Uncertainties represent one standard deviation from the mean value.

^aNet CO₂ flux of terrestrial biosphere.

^bNet CO₂ flux of terrestrial biosphere, including the contribution from the oxidation of reduced carbon.

^cEast Asia, including China, Japan, North and South Korea, and Mongolia.

^dEnsemble model median and range.

Understanding the CO₂ flux distributions

In the absence of independent downwind data that are sensitive to our a posteriori changes in Chinese CO₂ fluxes, we also infer independent CO₂ flux estimates from satellite column observations of CO₂ from the Japanese Greenhouse gases Observing Satellite (GOSAT)²¹ and the NASA Orbiting Carbon Observatory (OCO-2) (see Methods). Using these satellite data, we find that a posteriori CO₂ fluxes during the growing season (May to September) show larger uptake over central, northeast and southern parts of China than SR-1, consistent with the SR-2 inversion (Extended Data Fig. 3). Differences between these flux estimates can be partly explained by seasonal changes in clear-sky views (Extended Data Fig. 4) that are determined by cloud cover and aerosol loading. We find major data gaps over China in winter, where the a priori information plays a larger part in the a posteriori solution (Extended Data Fig. 5).

Using reports from quinquennial Chinese forest inventories²², we find that, since the 1990s, northeast and southwest China have experienced a period of rapid growth in forest area (Extended Data Fig. 6, Extended Data Table 1), reflecting national policies²³. These findings are supported by remote-sensing observations of land cover (Extended Data Fig. 7), vegetation indices (Fig. 3a, Extended Data Fig. 8, Supplementary Figs. 11, 12) and above-ground biomass (Fig. 3b) that show small but significant upward trends. A consequence of the rapid increase of afforestation during the past 30 years is that Chinese forests contain a large fraction of young and mid-aged trees (Extended Data Fig. 9), which are associated with a high rate of carbon sequestration^{6,20,24,25}.

The southwest region, in particular the Guangxi autonomous region, is populated by eucalyptus, which is a fast-growing and high-yielding tree species with high potential biomass carbon sequestration²⁶. These eucalyptus plantations are irrigated and fertilized, factors that would need to be considered in the overall environmental value of this carbon

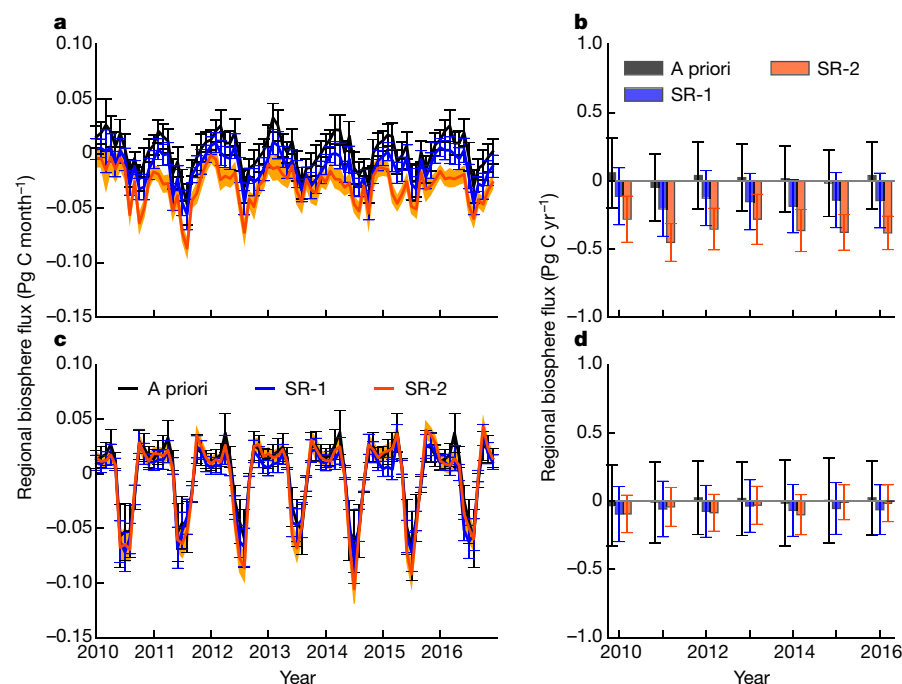


Fig. 2 | Terrestrial biosphere CO₂ fluxes. **a, b**, Over northeast China (within 38–54° N, 120–135° E); **c, d**, over southwest China (within 18–30° N, 95–110° E). Monthly CO₂ fluxes (Pg C month⁻¹) from the a priori inventory and a posteriori fluxes inferred from SR-1 and SR-2 are shown from 2010 to 2016 over northeast China (**a**) and southwest China (**c**); and corresponding annual fluxes (Pg C yr⁻¹) over northeast China (**b**) and southwest China (**d**). Vertical bars and the orange envelope (**a** and **c**) denote a priori and a posteriori uncertainties.

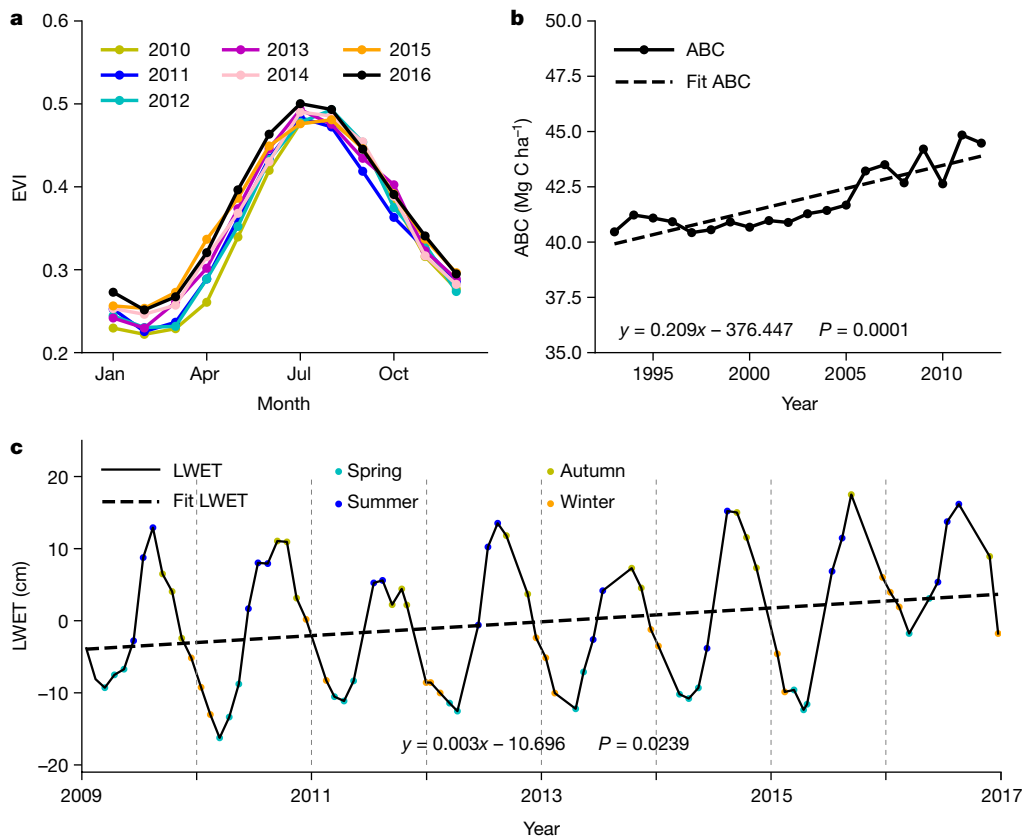


Fig. 3 | Satellite observations relating to vegetation growth. **a**, Leaf phenology: successive years (2010–2016) of superimposed monthly EVI from MODIS. **b**, Above-ground biomass harmonized from several sensors (1993–2012). **c**, Liquid water equivalent thickness (LWET) from the Gravity Recovery and Climate Experiment (GRACE) (2009–2016) over southwest China (18–30° N, 95–110° E). Data record lengths vary according to the sensor lifetime. The linear best-fit lines (dashed lines) and the associated *P* values are shown in **b** and **c**. More detailed data descriptions can be found in Supplementary Information.

sink. Correlative satellite data of leaf phenology and groundwater (Fig. 3, Supplementary Information) clearly show upward trends that together are consistent with a progressively larger biological carbon sink. Because it is a managed ecosystem, the southwest region appears to be insensitive to wider changes in climate (Supplementary Figs. 13, 14), particularly during the 2009–2010 drought associated with reduced precipitation²⁷.

We have shown that using atmospheric CO₂ measurements collected at a small number of additional sites changes our understanding of the distribution of CO₂ fluxes over China. This reflects the sparse and uneven distribution of ground-based measurements. Our use of satellite observations to verify a posteriori fluxes inferred from the in situ data will enable extensive improvement in CO₂ monitoring.

Online content

Any methods, additional references, Nature Research reporting summaries, source data, extended data, supplementary information, acknowledgements, peer review information; details of author contributions and competing interests; and statements of data and code availability are available at <https://doi.org/10.1038/s41586-020-2849-9>.

1. Le Quéré, C. et al. Global carbon budget 2018. *Earth Syst. Sci. Data* **10**, 2141–2194 (2018).
2. Peylin, P. et al. Global atmospheric carbon budget: results from an ensemble of atmospheric CO₂ inversions. *Biogeosciences* **10**, 6699–6720 (2013).
3. Thompson, R. L. et al. Top-down assessment of the Asian carbon budget since the mid 1990s. *Nat. Commun.* **7**, 10724 (2016).
4. Jiang, F. et al. A comprehensive estimate of recent carbon sinks in China using both top-down and bottom-up approaches. *Sci. Rep.* **6**, 22130 (2016).
5. Pan, Y. et al. A large and persistent carbon sink in the world's forests. *Science* **333**, 988–993 (2011).
6. Zhang, Y., Yao, Y., Wang, X., Liu, Y. & Piao, S. Mapping spatial distribution of forest age in China. *Earth Space Sci.* **4**, 108–116 (2017).
7. Williams, R. A. Mitigating biodiversity concerns in eucalyptus plantations located in South China. *J. Biosci. Med.* **3**, 57099 (2015).
8. Barlow, J. M., Palmer, P. I., Bruhwiler, L. M. & Tans, P. Analysis of CO₂ mole fraction data: first evidence of large-scale changes in CO₂ uptake at high northern latitudes. *Atmos. Chem. Phys.* **15**, 13739–13758 (2015).
9. Schimel, D. S. et al. Recent patterns and mechanisms of carbon exchange by terrestrial ecosystems. *Nature* **414**, 169–172 (2001).

10. Takahashi, T. et al. Climatological mean and decadal change in surface ocean pCO₂, and net sea-air CO₂ flux over the global oceans. *Deep Sea Res. II* **56**, 554–577 (2009).
11. Rödenbeck, C. et al. Data-based estimates of the ocean carbon sink variability — first results of the Surface Ocean pCO₂ Mapping intercomparison (SOCOM). *Biogeosciences* **12**, 7251–7278 (2015).
12. Gregg, J. S., Andres, R. J. & Marland, G. China: emissions pattern of the world leader in CO₂ emissions from fossil fuel consumption and cement production. *Geophys. Res. Lett.* **35**, L08806 (2008).
13. Liu, Z. et al. Reduced carbon emission estimates from fossil fuel combustion and cement production in China. *Nature* **524**, 335–338 (2015).
14. Piao, S. L. et al. The carbon budget of terrestrial ecosystems in East Asia over the last two decades. *Biogeosciences* **9**, 3571–3586 (2012).
15. Piao, S. et al. The carbon balance of terrestrial ecosystems in China. *Nature* **458**, 1009–1013 (2009).
16. Tian, H. et al. Net exchanges of CO₂, CH₄, and N₂O between China's terrestrial ecosystems and the atmosphere and their contributions to global climate warming. *J. Geophys. Res. Atmos.* **116**, G02011 (2011).
17. Zhang, H. et al. Net terrestrial CO₂ exchange over China during 2001–2010 estimated with an ensemble data assimilation system for atmospheric CO₂. *J. Geophys. Res. Atmos.* **119**, 3500–3515 (2014).
18. Wang, Q. et al. Primary estimation of Chinese terrestrial carbon sequestration during 2001–2010. *Sci. Bull.* **60**, 577–590 (2015).
19. Fang, J. Y., Chen, A. P., Peng, C. H., Zhao, S. Q. & Ci, L. Changes in forest biomass carbon storage in China between 1949 and 1998. *Science* **292**, 2320–2322 (2001).
20. Pan, Y., Luo, T., Birdsey, R., Hom, J. & Melillo, J. New estimates of carbon storage and sequestration in China's forests: effects of age-class and method on inventory-based carbon estimation. *Clim. Change* **67**, 211–236 (2004).
21. Yokota, T. et al. Global concentrations of CO₂ and CH₄ retrieved from GOSAT: first preliminary results. *Sci. Online Lett. Atmos.* **5**, 160–163 (2009).
22. Zeng, W., Tomppo, E., Healey, S. P. & Gadaw, K. V. The national forest inventory in China: history — results — international context. *For. Ecosyst.* **2**, 23 (2015).
23. Liu, J., Li, S., Ouyang, Z., Tam, C. & Chen, X. Ecological and socioeconomic effects of China's policies for ecosystem services. *Proc. Natl. Acad. Sci. USA* **105**, 9477–9482 (2008).
24. Wang, S. et al. Relationships between net primary productivity and stand age for several forest types and their influence on China's carbon balance. *J. Environ. Manage.* **92**, 1651–1662 (2011).
25. Yu, Y. et al. Influence of site index on the relationship between forest net primary productivity and stand age. *PLoS One* **12**, e0177084 (2017).
26. Du, H. et al. Carbon storage in a eucalyptus plantation chronosequence in Southern China. *Forests* **6**, 1763–1778 (2015).
27. Xu, K., Yang, D., Xu, X. & Lei, H. Copula based drought frequency analysis considering the spatio-temporal variability in Southwest China. *J. Hydrol.* **527**, 630–640 (2015).

Publisher's note Springer Nature remains neutral with regard to jurisdictional claims in published maps and institutional affiliations.

© The Author(s), under exclusive licence to Springer Nature Limited 2020

Methods

Data

In situ CO₂ mole fraction observations. We use (weekly) discrete flask air samples from 105 sites and (hourly) continuous observations from 52 sites that are part of the global atmospheric surface CO₂ observations network. These are currently described by the Observation Package (ObsPack) obspack_co2_1_GLOBALVIEWplus_v4.1_2018-10-29 data product²⁸ from NOAA's ESRL. We also use an additional Chinese data from WDCGG at Hok Tsui (HKG) provided by Hong Kong Observatory.

We use CO₂ mole fraction data from nine towers collected by the Japan–Russia Siberia Tall Tower Inland Observation Network (JR-STATION; Supplementary Table 1, Extended Data Fig. 1) over Siberia from 2009–2016^{29,30}. We also use weekly flask measurements and hourly continuous CO₂ mole fraction measurements during 2009–2016 of six new regional background sites over China (Longfengshan, Shangdianzi, Linan, Shangri-La, Jinsha and Akedala) (Supplementary Table 2, Extended Data Fig. 1) are operated by the China Meteorological Administration^{31,32}. Further details about these CO₂ observations are in Supplementary Information.

GOSAT observations. We use column CO₂ data collected by GOSAT, launched in January 2009 in a Sun-synchronous orbit with a local overpass time over China around 13:00³³. We use total column CO₂ (XCO₂) full-physics retrievals from GOSAT: v7.3 data product from the Atmospheric CO₂ Observations from Space (ACOS) from the Jet Propulsion Laboratory³⁴.

OCO-2 observations. We use column CO₂ data collected by NASA's OCO-2, launched in July 2014 in a sun-synchronous orbit with a local crossing time over China around 13:30³⁵. We use bias-corrected OCO-2 V8r data³⁶ in this study. We use only nadir observations over land with a warning level <12. After considering observation error correlations, we have thinned the data with a frequency of 0.1 Hz, corresponding to an approximate distance of 75 km between successive measurements.

NDVI and EVI represent composite properties of leaf area, chlorophyll and canopy structure. We use MOD13C2 (MODIS/Terra Vegetation Indices Monthly L3 Global 0.05° CMG V006)³⁷ to get NDVI AND EVI information. The data are only retained with pixel reliability values masked as good data ('0') or marginal data ('1').

GRACE provides information about changes in the water column^{38–40}. Rooting depths of Chinese terrestrial ecosystems are likely to be sufficiently deep that we cannot establish a direct and immediate relationship between vegetation and changes in precipitation. Changes in gravity due to changes in water column depth provide a much stronger relationship with vegetation access to water. We use the surface mass change data based on the RL05 spherical harmonics from the Center for Space Research at University of Texas, Austin (CSR), Jet Propulsion Laboratory (JPL) and Geoforschungs Zentrum Potsdam (GFZ). The three different processing groups chose different parameters and solution strategies when deriving month-to-month gravity field variations from GRACE observations. We use the ensemble mean of the three data fields and multiply the data by the scaling grid provided.

Above-ground biomass carbon. We use above-ground biomass carbon (ABC) estimates (1993–2012) based on harmonized vegetative optical depth data for 1993 onwards derived from a series of passive microwave satellite sensors⁴¹. These sensors include the Special Sensor Microwave Imager (SSM/I), Advanced Microwave Scanning Radiometer for Earth Observation System (AMSR-E), FengYun-3B Microwave Radiometer Imager (MWRI) and Windsat.

Models

To describe the relationship between surface fluxes of CO₂ and atmospheric CO₂, we use the GEOS-Chem global 3-D chemistry transport model (v9.02). For our experiments we run GEOS-Chem with a

horizontal resolution of 4° (latitude) × 5° (longitude), driven by the GEOS-5 (GEOS-FP from 2013) meteorological analyses from the Global Modelling and Assimilation Office Global Circulation Model based at NASA Goddard Space Flight Centre.

To describe atmospheric CO₂, we use well established emission inventories as our a priori flux estimates: (1) weekly biomass burning emissions⁴²; (2) monthly anthropogenic emissions^{43–45} (we use 88% of ODIAC anthropogenic^{43,44} inventory in this study, details in Supplementary Information); (3) monthly climatological ocean fluxes¹⁰; and (4) three-hourly terrestrial biosphere fluxes⁴⁶.

We use an ensemble Kalman Filter (EnKF) framework^{47–49} to infer CO₂ fluxes from the in situ or space-based measurements of atmospheric CO₂ concentrations. Surface flux $f^a(x, t)$ (in kg m⁻² s⁻¹) at location x and time t is given by^{47,49}:

$$f^a(x, t) = f^0(x, t) + \sum_i^N c_i BF_i(x, t),$$

where $f^0(x, t)$ describes the a priori estimates (in kg m⁻² s⁻¹). The basis function set $BF_i(x, t)$ is defined as the pulse-like (monthly) CO₂ fluxes over pre-defined geographical regions (in kg m⁻² s⁻¹). For each individual basis function, we estimate the unitless scaling coefficient c_i by optimally fitting the model to observation data. The coefficients for the basis function set represent the state vector \mathbf{c} .

We use a total of 792 monthly basis functions split between 317 oceanic regions and 475 land regions. These regions are based on established 22 regions in TransCom-3⁵⁰. To infer Chinese CO₂ fluxes on a spatial resolution of 4° (latitude) × 5° (longitude) we further divide the Eurasia temperate region into 78 sub-regions.

We solve for the a posteriori state vector using the Kalman gain matrix K :

$$\mathbf{c}_a = \mathbf{c}_0 + K(\mathbf{y}_{\text{obs}} - H(\mathbf{c}_0)),$$

where \mathbf{c}_a and \mathbf{c}_0 represent the a priori and a posteriori estimates, respectively; \mathbf{y}_{obs} denotes the atmospheric CO₂ observations; and H describes the observation operator that relates surface fluxes to the observation data. In our case, H represents the GEOS-Chem model sampled at measurement locations, and in the case of satellite data also taking into account instrument sensitivity to CO₂.

We assume a 50% uncertainty for monthly land terrestrial fluxes, and 40% for monthly ocean fluxes⁴⁹. We assume land (ocean) a priori fluxes are correlated with a correlation length of 500 (800) km.

We determine the terrestrial biosphere flux by subtracting the fossil fuel and cement production emission estimate (FF). This is a common approach^{2–4,51}, based on an assumption about our knowledge of FF flux. Consequently, our biosphere fluxes depend to a certain degree on what we assume for anthropogenic emissions (Supplementary Table 3).

In addition to our control run (SR-2), we also report Chinese land biosphere fluxes that correspond to the ODIAC anthropogenic inventory^{43,44}. We find that our total net a posteriori emissions of CO₂ over China (1.35 ± 0.38 Pg C yr⁻¹) are not significantly different to our control inversion (1.37 ± 0.38 Pg C yr⁻¹), suggesting that our a posteriori fluxes are robust. However, our a posteriori land biosphere fluxes represent a larger sink of CO₂ (−1.47 ± 0.38 Pg C yr⁻¹) compared to our control flux estimates (−1.11 ± 0.38 Pg C yr⁻¹). Our larger a posteriori sink estimate is expected since we are subtracting a larger FF flux from the net emission estimate. This calculation also provides a crude measure of the land biosphere flux uncertainty due to uncertainties in FF fluxes.

In the EnKF framework, the Kalman gain matrix K is approximated by⁴⁶:

$$K \approx \Delta C \Delta Y^T (\Delta Y \Delta Y^T + R)^{-1},$$

where R is the observation error covariance matrix. ΔC represents the ensemble of perturbations to the state vector that are used to construct

the a priori error covariance, $P \approx \Delta C \Delta C^T$ where T denotes the matrix transpose⁴⁷. To compare with observation, ΔC is projected onto observation space using the observation operator $\Delta Y = H(\Delta C)$. We assume no observation error correlations but include an additional 1.0 parts per million uncertainty to the reported observation errors to account for model transport errors.

The methodology we use to estimate annual uncertainty estimates from the ensemble Kalman filter with a lagged window is described in detail in Supplementary Information.

Data availability

GRACE data are available from <http://grace.jpl.nasa.gov>. ABC data are available from <https://www.wenfo.org/wald/global-biomass>. The NDMI, EVI and LAI data were retrieved from the online Data Pool, courtesy of the NASA Land Processes Distributed Active Archive Center, USGS/Earth Resources Observation and Science Center (https://lpdaac.usgs.gov/data_access/data_pool). CO₂ mole fraction data from the Chinese sites used in this study are available at <https://doi.org/10.17632/w3bwmr6rfg.1> on <http://data.mendeley.com>. Requests for further information about these data should be directed to S.F. Source data are provided with this paper.

Code availability

We acknowledge the Python Software Foundation: Python Language Reference, version 3.7.7; available at <http://www.python.org>. We also acknowledge Matplotlib (v3.1.3, 10.5281/zenodo.3984190)⁵². The community-led GEOS-Chem model of atmospheric chemistry and transport is maintained centrally by Harvard University (<http://acmg.seas.harvard.edu/geos/>) and is available on request. The ensemble Kalman filter code is publicly available as PyOSSE (<https://www.nceo.ac.uk/data-tools/atmospheric-tools/>).

28. Cooperative Global Atmospheric Data Integration Project. Multi-laboratory compilation of atmospheric carbon dioxide data for the period 1957–2017; obspack_co2_1_GLOBALVIEWplus_v4.1_2018_10_29 (NOAA Earth System Research Laboratory, Global Monitoring Division, 2018); <https://doi.org/10.25925/20181026>
29. Sasakawa, M. et al. Continuous measurements of methane from a tower network over Siberia. *Tellus B* **62**, 403–416 (2010).
30. Saeki, T. et al. Carbon flux estimation for Siberia by inverse modeling constrained by aircraft and tower CO₂ measurements. *J. Geophys. Res. Atmos.* **118**, 1100–1122 (2013).
31. Fang, S. X. et al. In situ measurement of atmospheric CO₂ at the four WMO/GAW stations in China. *Atmos. Chem. Phys.* **14**, 2541–2554 (2014).
32. Fang, S. X., Tans, P. P., Steinbacher, M., Zhou, L. X. & Luan, T. Comparison of the regional CO₂ mole fraction filtering approaches at a WMO/GAW regional station in China. *Atmos. Meas. Tech.* **8**, 5301–5313 (2015).
33. Kuze, A., Suto, H., Nakajima, M. & Hamazaki, T. Thermal and near infrared sensor for carbon observation Fourier-transform spectrometer on the Greenhouse Gases Observing Satellite for greenhouse gases monitoring. *Appl. Opt.* **48**, 6716–6733 (2009).
34. OCO-2 Science Team. ACOS GOSAT/TANSO-FTS ACOS Level 2 Bias-Corrected XCO₂ and Other Select Fields from the Full-Physics Retrieval Aggregated as Daily Files V7.3 (GES DISC, 2016); https://disc.gsfc.nasa.gov/datacollection/ACOS_L2_Lite_FP_7.3.html (accessed October 2017).
35. Eldering, A. et al. The Orbiting Carbon Observatory-2 early science investigations of regional carbon dioxide fluxes. *Science* **358**, eaam5745 (2017).
36. OCO-2 Science Team. OCO-2 Level 2 Bias-Corrected XCO₂ and Other Select Fields from the Full-Physics Retrieval Aggregated as daily files. *Retrospective Processing V8r* (GES DISC, 2017); <https://doi.org/10.5067/W8QGIYNKS3JC>

37. Didan, K. MOD13C2 MODIS/Terra Vegetation Indices Monthly L3 Global 0.05 Deg CMG V006 (NASA EOSDIS Land Processes DAAC, 2015); <https://doi.org/10.5067/modis/mod13c2.006>
38. Swenson, S. & Wahr, J. Post-processing removal of correlated errors in GRACE data. *Geophys. Res. Lett.* **33**, L08402 (2006).
39. Swenson, S. C. GRACE Monthly Land Water Mass Grids NETCDF Release 5.0 V5.0 (PODAAC, 2012); <https://doi.org/10.5067/TELND-NC005> (accessed 27 September 2017).
40. Landerer, F. W. & Swenson, S. C. Accuracy of scaled GRACE terrestrial water storage estimates. *Water Resour. Res.* **48**, W04531 (2012).
41. Liu, Y. Y. et al. Recent reversal in loss of global terrestrial biomass. *Nat. Clim. Change* **5**, 470–474 (2015).
42. van der Werf, G. R. et al. Global fire emissions and the contribution of deforestation, savanna, forest, agricultural, and peat fires (1997–2009). *Atmos. Chem. Phys.* **10**, 11707–11735 (2010).
43. Oda, T. & Maksyutov, S. A very-high-resolution (1 km × 1 km) global fossil fuel CO₂ emission inventory derived using a point source database and satellite observations of nighttime lights. *Atmos. Chem. Phys.* **11**, 543–556 (2011).
44. Oda, T. et al. China CO₂ emission accounts 1997–2015. *Sci. Data* **5**, 170201 (2018). <https://doi.org/10.17595/20170411.001> (accessed 1 June 2017).
45. Shan, Y. et al. China CO₂ emission accounts 1997–2015. *Sci. Data* **5**, 170201 (2018).
46. Olsen, S. C. & Randerson, J. T. Differences between surface and column atmospheric CO₂ and implications for carbon cycle research. *J. Geophys. Res. Atmos.* **109**, D02301 (2004).
47. Feng, L., Palmer, P. I., Bösch, H. & Dance, S. Estimating surface CO₂ fluxes from space-borne CO₂ dry air mole fraction observations using an ensemble Kalman filter. *Atmos. Chem. Phys.* **9**, 2619–2633 (2009).
48. Feng, L. et al. Evaluating a 3-D transport model of atmospheric CO₂ using ground-based, aircraft, and space-borne data. *Atmos. Chem. Phys.* **11**, 2789–2803 (2011).
49. Feng, L. et al. Estimates of European uptake of CO₂ inferred from GOSAT XCO₂ retrievals: sensitivity to measurement bias inside and outside Europe. *Atmos. Chem. Phys.* **16**, 1289–1302 (2016).
50. Gurney, K. R. et al. Towards robust regional estimates of CO₂ sources and sinks using atmospheric transport models. *Nature* **415**, 626–630 (2002).
51. Saeki, T. & Patra, P. K. Implications of overestimated anthropogenic CO₂ emissions on East Asian and global land CO₂ flux inversion. *Geosci. Lett.* **4**, 9 (2017).
52. Hunter, J. D. Matplotlib: a 2D graphics environment. *Comput. Sci. Eng.* **9**, 90–95 (2007).

Acknowledgements J.W. acknowledges support by the Strategic Priority Research Program of Chinese Academy of Sciences (grant no. XDA17010100) and funding from the UK Natural Environmental Research Council (NERC) National Centre for Earth Observation (NCEO). L.F., P.I.P. and H.B. are supported by the NERC NCEO (grant no. NE/R016518/1). H.B. acknowledges funding from the ESA CCI and C3S projects. P.I.P. also acknowledges funding from a Royal Society Wolfson Research Merit Award. Y.L. is supported by the international partnership programme of the Chinese Academy of Sciences (grant no. 134111KYB20170010). S.F. is supported by the National Key Research and Development Program of China (grant no. 2017YFC0209700). D.Y. is supported by the National Key Research and Development Program of China (grant no. 2016YFA0600203). C.W.O. was supported by subcontracts from the OCO-2 project at the NASA Jet Propulsion Laboratory. J.W., L.F., P.I.P., Y.L., H.B. and D.Y. acknowledge funding from the ESA-MOST Dragon 3 Cooperation Programme. We gratefully acknowledge all CO₂ ground observations contributors to the obspack_co2_1_GLOBALVIEWplus_v4.1_2018-10-29 and to NOAA ESRL for maintaining this database. We also acknowledge data provided by Hong Kong Observatory, the Japan–Russia Siberia Tall Tower Inland Observation Network and the World Data Centre for Greenhouse Gases. We also thank P. Somkuti for GOSAT SIF data and the broader GOSAT team who provided the L1 data.

Author contributions Y.L., P.I.P. and L.F. designed the research. S.F. and L.L. processed and evaluated the observed data. J.W. and L.F. performed the atmospheric inversion analysis and data analysis. X.T. and C.X. provided the national forest inventory data. P.I.P. and J.W. led the writing of the paper, with contributions from L.F., Y.L., S.F., H.B., C.W.O., X.T., D.Y., L.L. and C.X.

Competing interests The authors declare no competing interests.

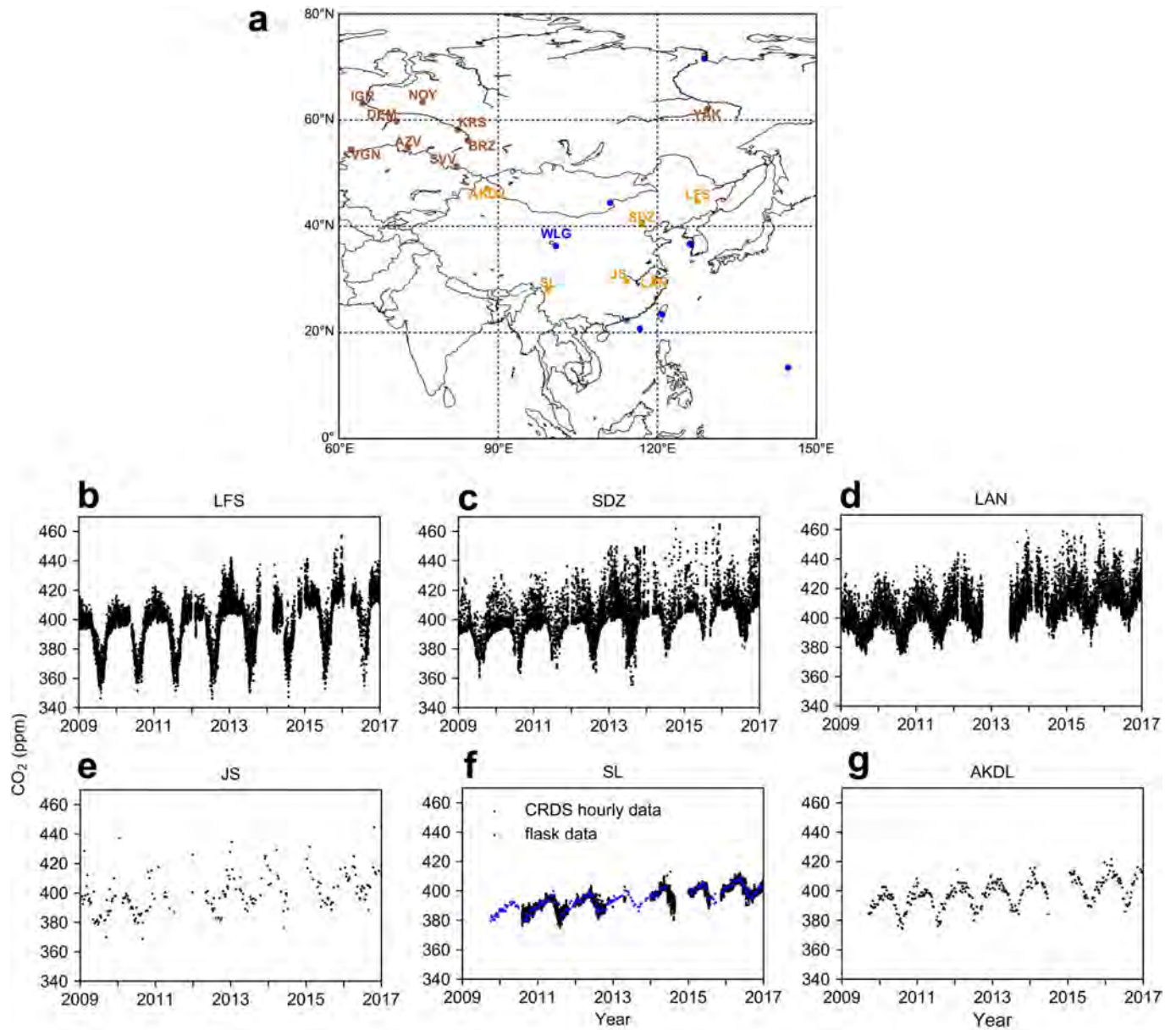
Additional information

Supplementary information is available for this paper at <https://doi.org/10.1038/s41586-020-2849-9>.

Correspondence and requests for materials should be addressed to P.I.P., Y.L. or S.F.

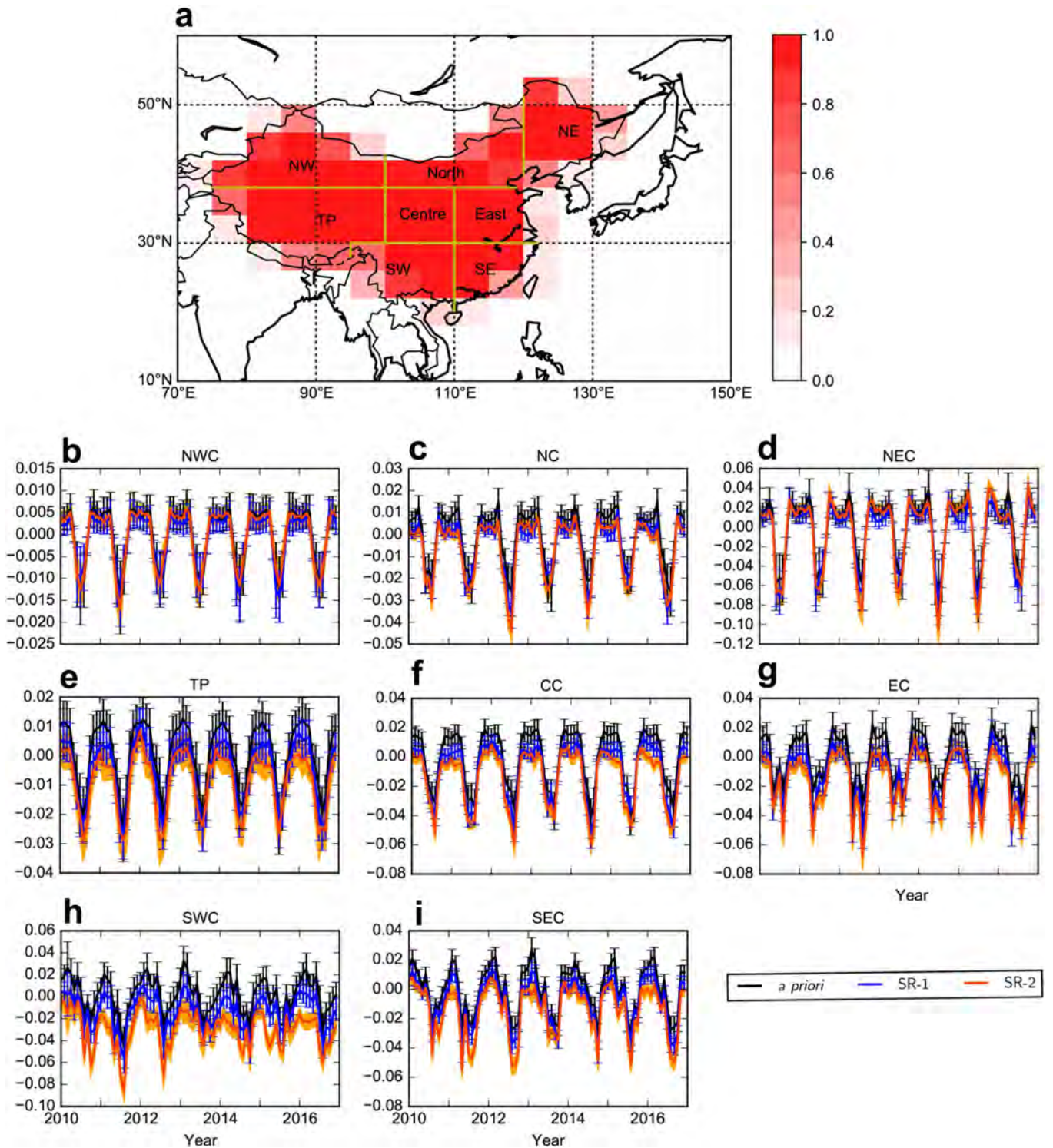
Peer review information Nature thanks Sourish Basu, Julia Marshall, Peter Rayner and the other, anonymous, reviewer(s) for their contribution to the peer review of this work.

Reprints and permissions information is available at <http://www.nature.com/reprints>.



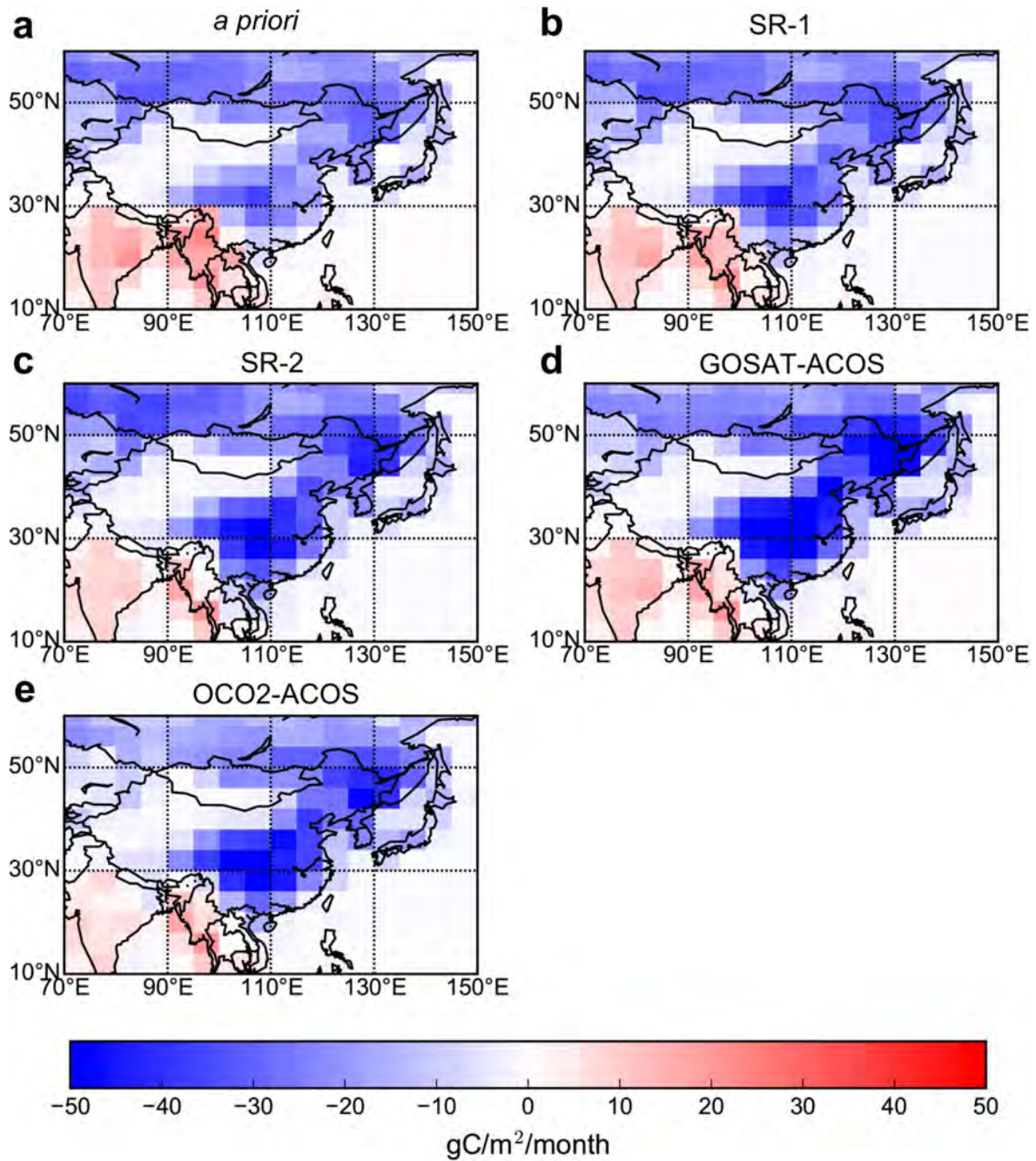
Extended Data Fig. 1 | In situ atmospheric CO₂ measurements across East Asia. **a**, Map showing the location of atmospheric CO₂ measurement sites over East Asia used in our numerical experiments. Coloured dots represent individual measurement sites referred to by letter codes (Supplementary Tables 1, 2). Blue dots represent NOAA ObsPack stations, the cyan dot represents the HKG station from WDCGG, brown dots represent Siberia

stations and orange dots represent CMA regional background stations. **b–g**, CO₂ mole fraction observations (in parts per million, ppm) at the six sites across China from 2009 to 2017 used in this study. Discrete (weekly) flask air samples, denoted by blue dots, and continuous (hourly) observations, denoted by black dots, are collected and analysed by the China Meteorological Administration. CRDS, cavity ring-down spectrometer.



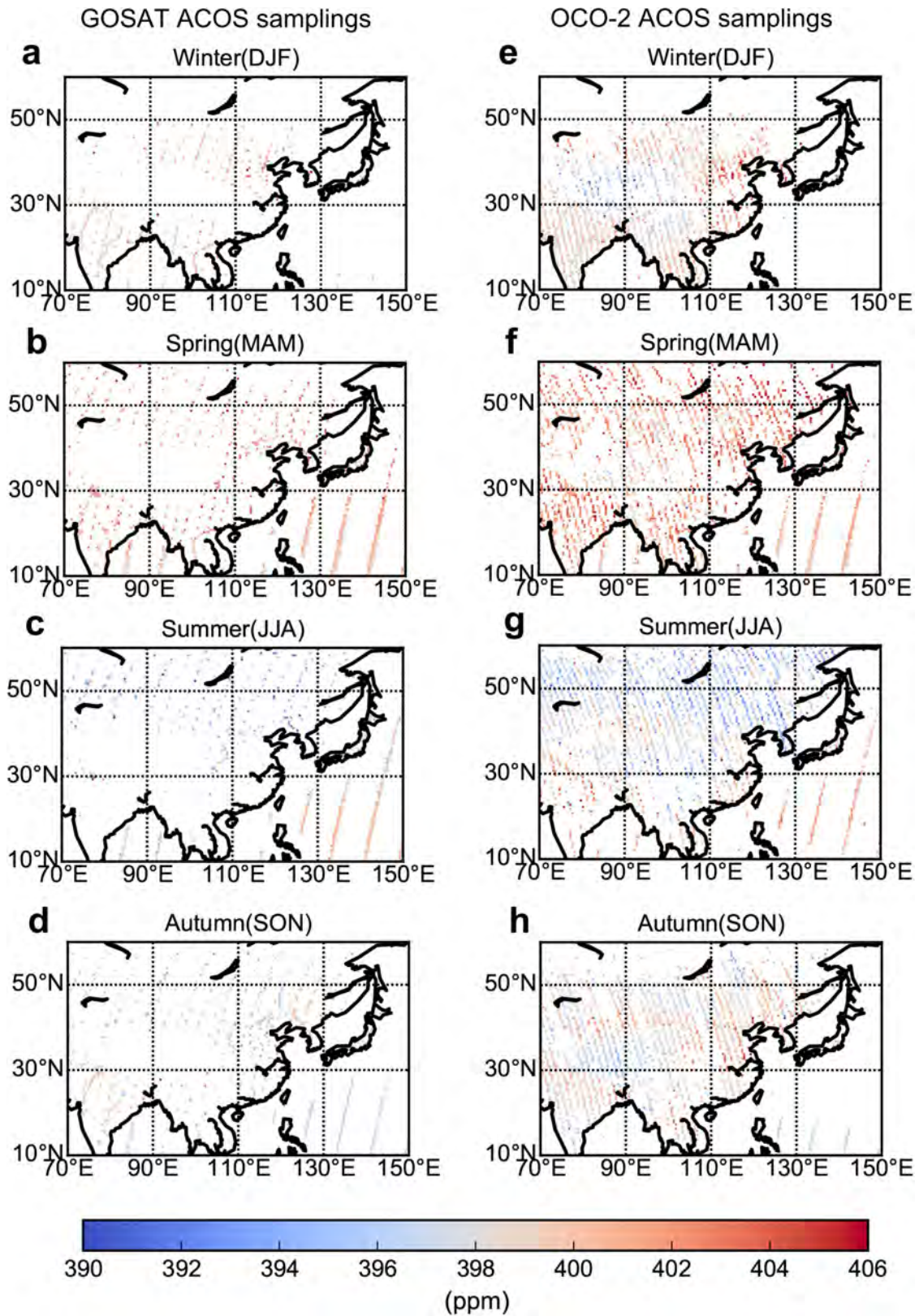
Extended Data Fig. 2 | Monthly subcontinental Chinese CO₂ flux estimates. **a**, Map showing the subcontinental geographical regions over China where we report a posteriori CO₂ fluxes. Colours denote the proportion of each region that falls within mainland China. **b–i**, Monthly regional a priori and a posteriori biosphere CO₂ fluxes (Pg C month⁻¹) over China during 2010–2016. A posteriori

fluxes are inferred from data used in the SR-1 and SR-2 inversions (see main text). Vertical bars and the orange envelope denote a priori and a posteriori uncertainties. NWC, northwest China; NC, northern China; NE, northeast China; TP, Tibetan Plateau; CC, central China; EC, eastern China; SW, southwest China; SE, southeast China, as shown in **a**.

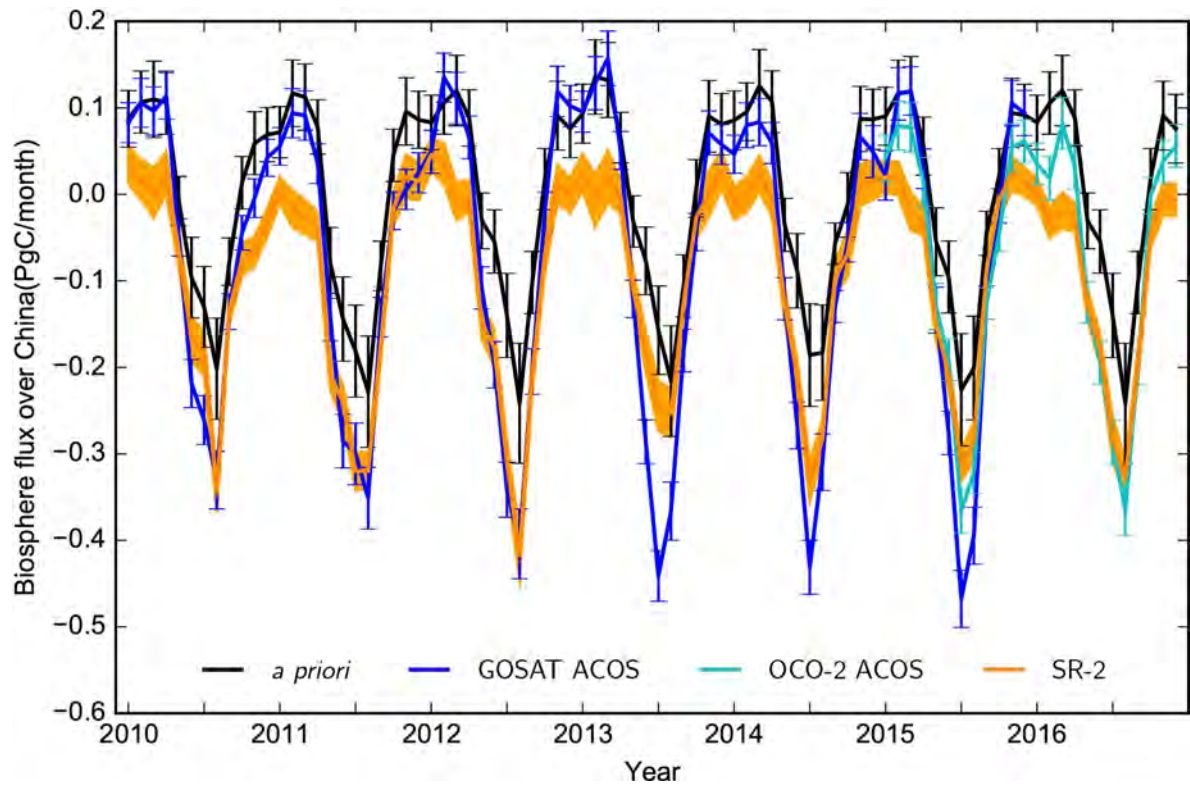


Extended Data Fig. 3 | Mean spatial distribution of a priori and a posteriori land biosphere CO₂ fluxes from May to September, inferred from in situ and satellite observations of CO₂. **a**, Our a priori fluxes. **b, c**, The a posteriori fluxes corresponding to inversions SR-1 and SR-2 (see main text) that use in situ

data. **d, e**, A posteriori fluxes inferred from column observations of CO₂ from GOSAT and from NASA's OCO-2, respectively. Flux estimates reported represent a temporal mean from 2010 to 2015, except for **e**, which is only for 2015.

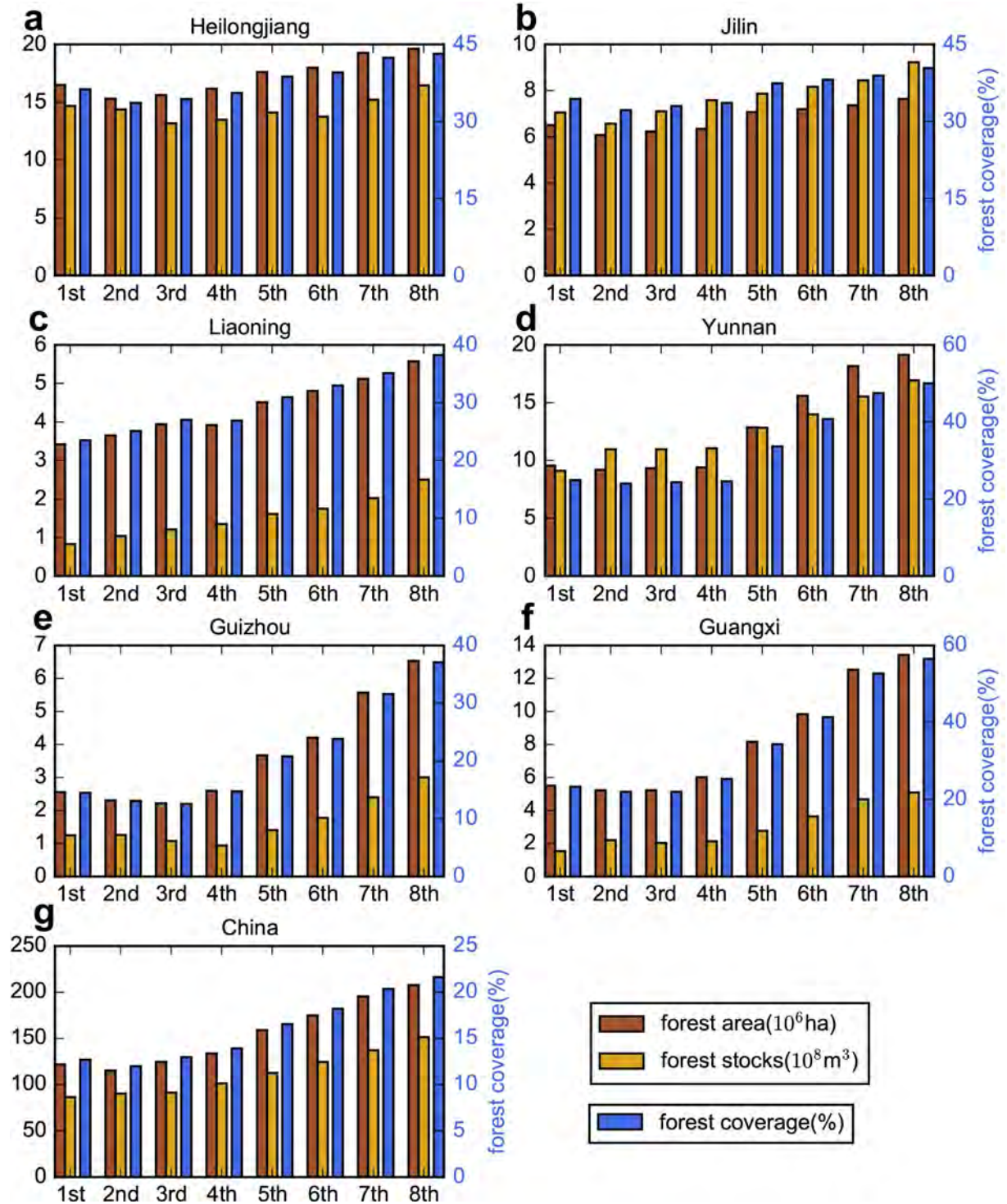


Extended Data Fig. 4 | Seasonal distribution and magnitude of satellite retrievals of column CO₂ from December 2014 to November 2015. a–d, Data from GOSAT (v7.3 ACOS). e–h, Data from OCO-2 (v8r). See Methods section ‘Data’ for further information.



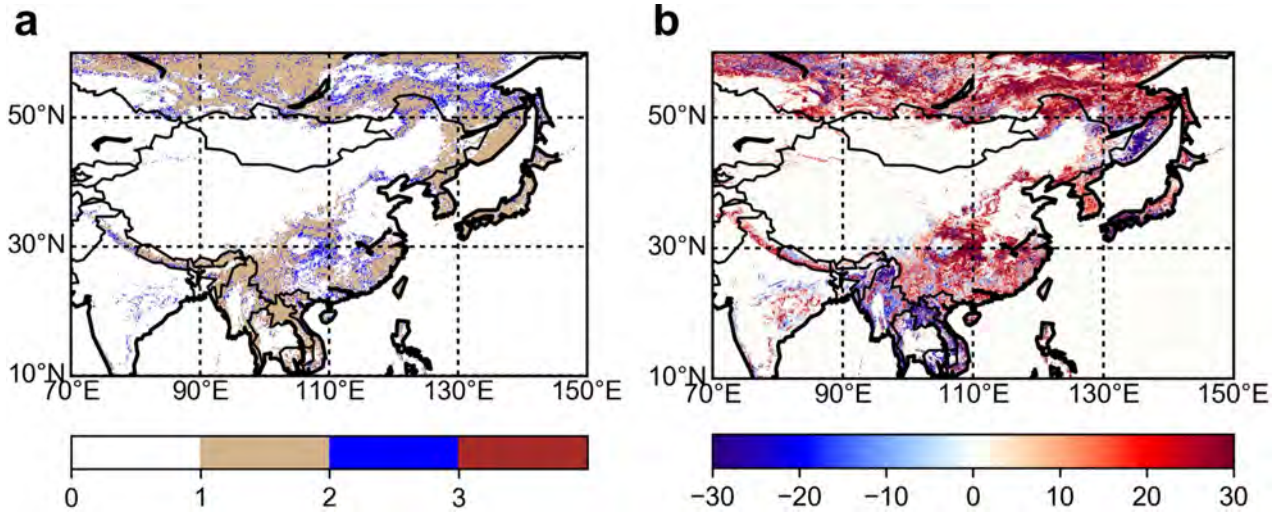
Extended Data Fig. 5 | A priori and a posteriori monthly biosphere CO₂ fluxes over China inferred from the GOSAT CO₂ column data and in situ data from 2010 to 2016. We also report a posteriori fluxes inferred from OCO-2 CO₂ column from September 2014 to December 2016. Vertical bars and shaded

envelopes denote a posteriori uncertainties. Higher annual fluxes inferred from GOSAT and OCO-2 are due mainly to higher a posteriori fluxes during winter months when data coverage is sparse (Extended Data Fig. 4) and the fluxes are more influenced by a priori values.



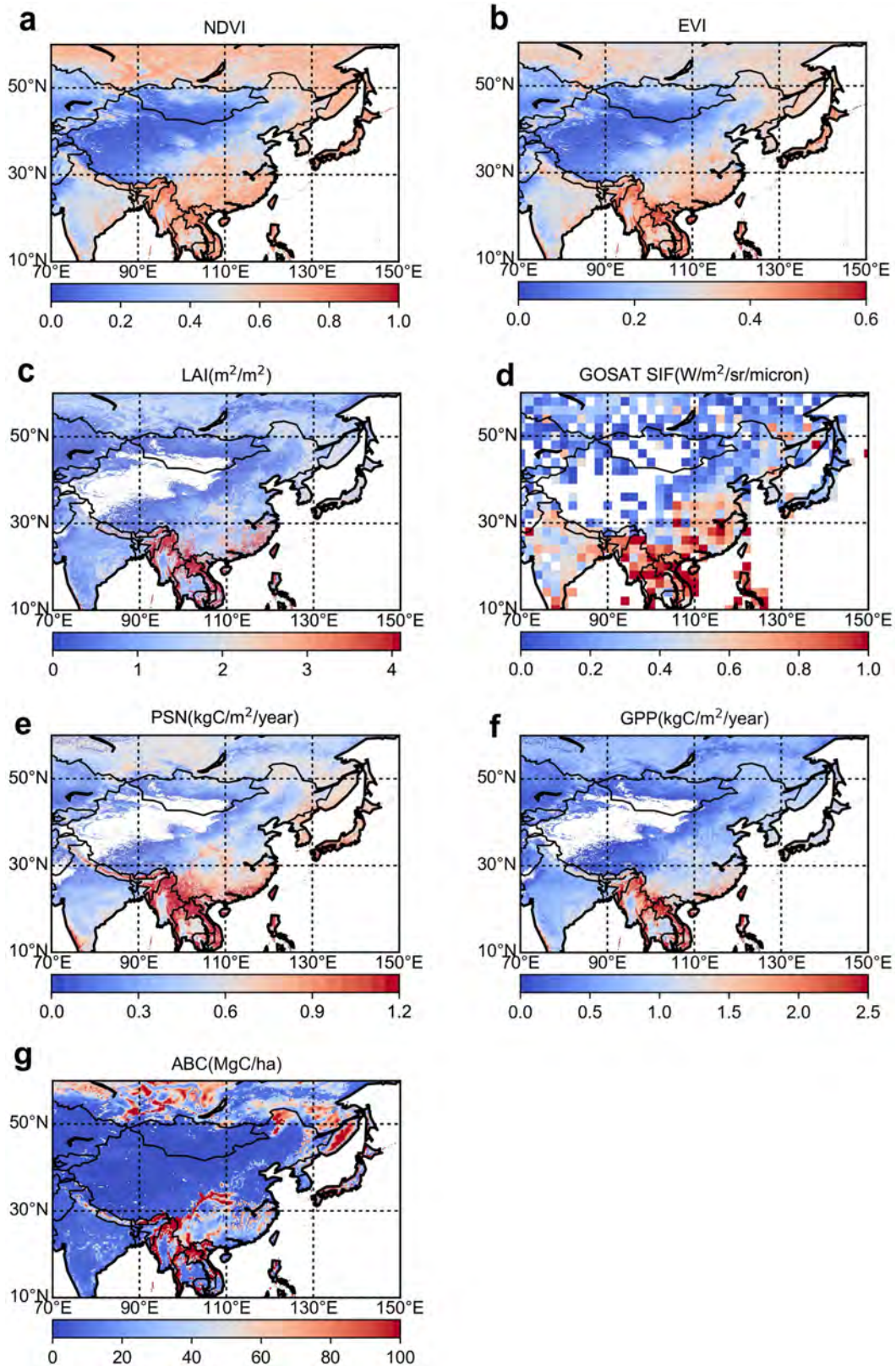
Extended Data Fig. 6 | Changes in forest area, forest stocks and forest coverage over six key forested Chinese provinces and over the whole of China, 1973–2013. a–f, Values for Heilongjiang, Jilin, Liaoning, Yunnan, Guizhou and Guangxi provinces. **g,** Values for China. The x-axis labels refer to

the National Forest Inventory of China's State Forestry Administration: 1st (1973–1976), 2nd (1977–1981), 3rd (1984–1988), 4th (1989–1993), 5th (1994–1998), 6th (1999–2003), 7th (2004–2008) and 8th (2009–2013).



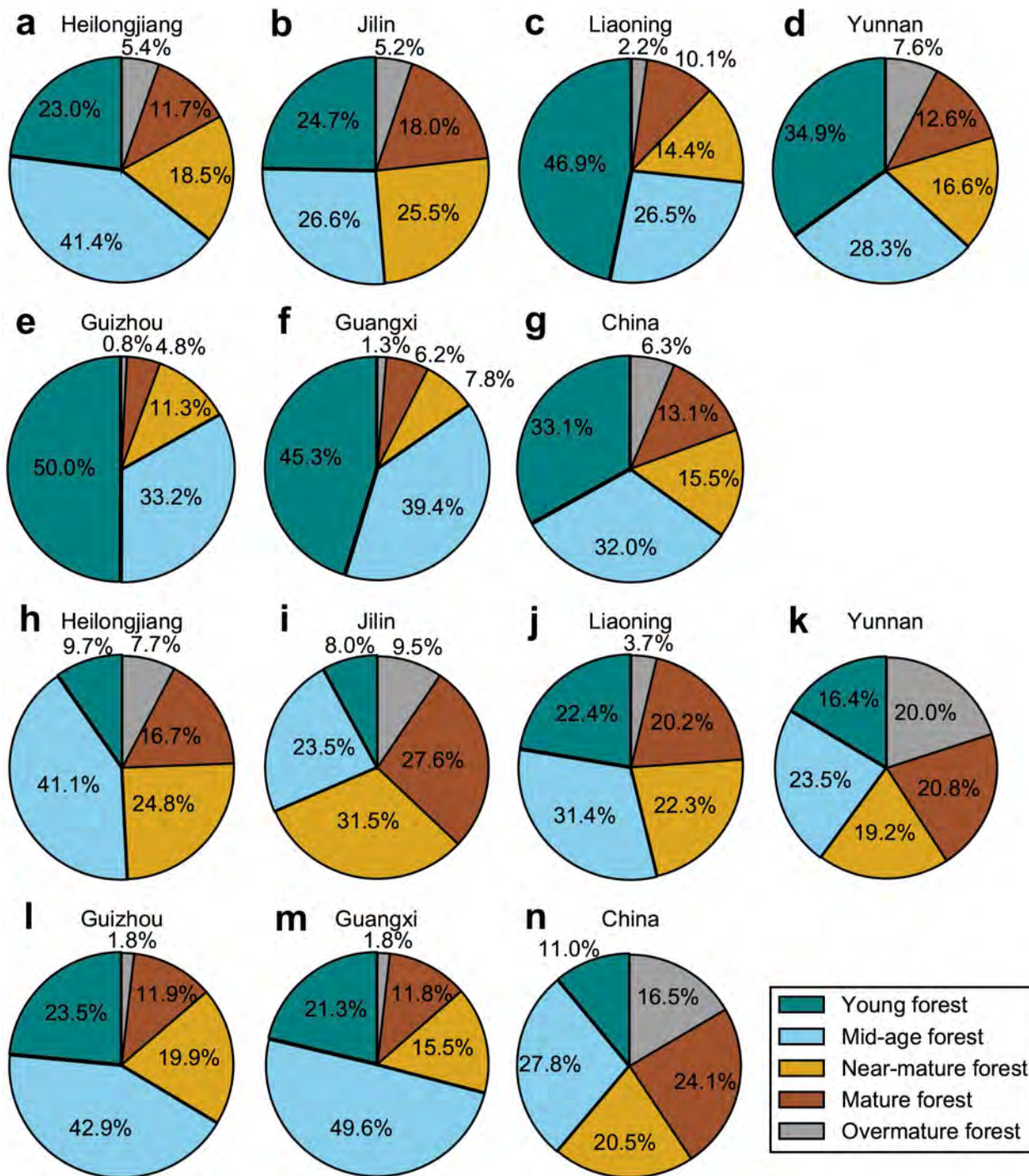
Extended Data Fig. 7 | Forest cover change over China during the period 2002–2012. **a**, How land cover changed from 2002 to 2012: 0 (1) denotes non-forest (forest) in both 2002 and 2012, 2 denotes conversion from non-forest to forest between 2002 and 2012, and 3 denotes conversion from

forest to non-forest between 2002 and 2012. **b**, The forest percentage change per grid box from 2002 to 2012. Data are presented on a $0.05^\circ \times 0.05^\circ$ spatial grid.



Extended Data Fig. 8 | Multi-year mean of satellite observations of vegetation indices. a, NDVI. b, EVI. c, LAI. d, Solar induced fluorescence (SIF). e, Net photosynthesis (PSN). f, Gross primary production (GPP).

g, Above-ground biomass carbon (ABC). See Supplementary Information for details. The mean is over 2010–2012, inclusive, for ABC, and over 2010–2016 for the other data.



Extended Data Fig. 9 | Forest area and stock of five forest-stand age groups over six key forested provinces and over the whole of China. a–f, Forest area for Heilongjiang, Jilin, Liaoning, Yunnan, Guizhou and Guangxi provinces. **g,** Forest area for China. **h–m,** Forest stock for Heilongjiang, Jilin, Liaoning, Yunnan, Guizhou and Guangxi provinces. **n,** Forest stock for China. Forest stands are divided into five age groups: young, mid-aged, near-mature, mature and overmature. Data are taken from the 8th NFI.

Yunnan, Guizhou and Guangxi provinces. **n,** Forest stock for China. Forest stands are divided into five age groups: young, mid-aged, near-mature, mature and overmature. Data are taken from the 8th NFI.

Extended Data Table 1 | Summary statistics calculated from the 6th to 8th (and 9th where available) National Forest Inventory of China's State Forestry Administration for China and six Chinese Provinces

Period	Forest land (10 ⁶ ha)	Forest stock (10 ⁶ m ³)	Plantation forest area (10 ⁶ ha)	Plantation forest stock (10 ⁶ m ³)	Fraction of planted forest area (%)	Fraction of planted forest stock (%)	Forest coverage (%)
China							
6 th (1999-2003)	171.1	12455.9	53.3	1504.5	31.1	12.1	18.2
7 th (2004-2008)	183.5	13720.8	61.7	1960.5	34.0	14.7	20.4
8 th (2009-2013)	193.3	15137.3	69.3	2483.3	36.3	16.8	21.6
Guangxi							
6 th (2000)	9.8	364.8	4.5	132.1	45.8	36.2	41.4
7 th (2005)	10.3	468.8	5.2	171.3	49.9	36.5	52.7
8 th (2010)	11.2	509.4	6.4	222.7	56.8	43.7	56.5
9 th (2015)	14.3	677.5	7.3	345.2	51.3	50.9	60.2
Yunnan							
6 th (2002)	15.0	1399.3	2.5	52.0	16.8	3.7	40.8
7 th (2007)	16.5	1553.8	3.3	72.6	19.8	4.7	47.5
8 th (2012)	17.5	1693.1	4.1	110.2	23.7	6.5	50.0
9 th (2016)	21.2	1894.9	5.3	262.1	24.8	13.8	59.3
Guizhou							
6 th (2000)	4.2	178.0	1.8	54.5	43.7	30.6	23.8
7 th (2005)	4.6	240.1	2.0	87.2	43.5	36.3	31.6
8 th (2010)	5.4	300.8	2.4	115.6	44.2	38.4	37.1
9 th (2015)	7.7	391.8	3.2	165.9	40.9	42.3	43.8
Heilongjiang							
6 th (2000)	17.98	1375.02	1.73	94.50	9.60	6.87	39.54
7 th (2005)	19.27	1521.05	2.36	135.20	12.23	8.89	42.39
8 th (2010)	19.62	1644.87	2.47	164.24	12.56	9.98	43.16
Jilin							
6 th (1999)	7.19	816.455	1.48	90.63	20.60	11.10	38.13
7 th (2004)	7.36	844.12	1.49	95.95	20.24	11.37	38.93
8 th (2009)	7.63	922.57	1.61	103.97	21.04	11.27	40.38
Liaoning							
6 th (2000)	4.64	174.77	2.68	63.10	57.66	36.11	32.97
7 th (2005)	4.84	202.27	2.83	72.99	58.53	36.09	35.13
8 th (2010)	5.17	250.46	3.07	94.88	59.37	37.88	38.24

The period defined for each China-wide census reflects the range of years of the individual provincial censuses.